DENTAL MATERIALS 35 (2019) 87–97

Available online at www.sciencedirect.com

ScienceDirect

journal homepage: www.intl.elsevierhealth.com/journals/dema

Exceptional contact elasticity of human enamel in nanoindentation test

Naofumi Shimomura[a], *Reina Tanaka*[b], *Yo Shibata*[b,c,*], *Zhongpu Zhang*[c], *Qing Li*[c], *Jun Zhou*[b,d], *Wurihan*[b], *Takuma Tobe*[b], *Sachiko Ikeda*[b], *Kazuko Yoshikawa*[e], *Yukie Shimada*[a], *Takashi Miyazaki*[b]

[a] *Department of Pediatric Dentistry, Showa University School of Dentistry, 2-1-1 Kitasenzoku, Ohta-ku, Tokyo 145-8515, Japan*

[b] *Department of Conservative Dentistry, Division of Biomaterials and Engineering, Showa University School of Dentistry, 1-5-8 Hatanodai, Shinagawa-ku, Tokyo 142-8555, Japan*

[c] *The University of Sydney, School of Aerospace, Mechanical and Mechatronic Engineering, NSW 2006, Australia*

[d] *School of Stomatology, Hospital of Stomatology, Tianjin Medical University, 12 Observatory Road, Tianjin 300070, China*

[e] *Department of Conservative Dentistry, Division of Aesthetic Dentistry and Clinical Cariology, Showa University School of Dentistry, 2-1-1 Kitasenzoku, Ohta-ku, Tokyo 145-8515, Japan*

ARTICLE INFO

Article history:
Received 14 July 2018
Received in revised form
27 October 2018
Accepted 1 November 2018

Keywords:
Enamel
Nanoindentation
Mechanical properties
Stress–strain behavior
Dynamic mechanical analysis
Resilience

ABSTRACT

Objective. Tooth enamel has unsurpassed hardness and stiffness among mammalian tissue structures. Such stiff materials are usually brittle, yet mature enamel can survive for a lifetime. Understanding the nanoscale origin of enamel durability is important for developing advanced load-bearing biomaterials. Here, nanoscale exceptional contact elasticity of the human tooth enamel, based on nanoindentation tests, is reported.

Methods. Spherical indenter tips with radii of 243 and 1041 nm were used to determine stress–strain curves of enamel. Force–displacement curves were recorded using quasi-static loading strain rates of 0.031, 0.041, and 0.061 s^{-1}. The storage moduli from a superimposed signal amplitude (dynamic strain at 220 Hz) embedded during primary quasi-static loading and from quasi-static elastic theory were simultaneously measured. Modulus mapping was considered to be an extremely low quasi-static loading strain rate indentation test.

Results. The elastic limits were 7–9 GPa and 5–6 GPa for the small and large indenters, respectively. The elastic–plastic transition point and elastic modulus value increased with substantially increased quasi-static loading strain rate. The results suggested that the increase of the elastic limit during high-loading strain was associated with exceptional contact elasticity at the nanoscale of the enamel structure and the consequent extension of the contact area (i.e., a temporary pile-up response, dependent on the enamel nanocrystals and protein glue).

Significance. Structural modification at this scale effectively prevents the initiation of cracking from localized strain, thus reinforcing the bulk structure. These results may provide valuable insight for conceptualizing bio-inspired nanocomposites.

* *Corresponding author at*: Department of Conservative Dentistry, Division of Biomaterials and Engineering, Showa University School of Dentistry, 1-5-8 Hatanodai, Shinagawa-ku, Tokyo 142-8555, Japan.
E-mail address: yookun@dent.showa-u.ac.jp (Y. Shibata).

https://doi.org/10.1016/j.dental.2018.11.005
0109-5641/

1. Introduction

Natural biominerals have long inspired researchers to conceptualize new functional materials for human health and industrial applications because the natural material characteristics that meet the multifunctional criteria are often superior to those of similar synthetic materials [1–3]. In particular, tooth enamel is the hardest and stiffest mineralized biological tissue, which allows it to exhibit remarkable resilience throughout the life of an individual, despite it comprising only the thin outer covering of the tooth [2].

It is likely that the intrinsic toughening mechanism of enamel depends, at least in part, on its multiscale dimensions, which include enamel rods surrounded by a protein-rich sheath layer [4]. Such inherent micron-scale structures in natural biominerals play an important role in producing interfaces that open up in the presence of potentially dangerous cracks, thus deflecting the crack and making its propagation energetically expensive [5]. Further characterization at the nanoscale (i.e., material) level can help to probe the local origins of enamel durability.

Recent evidence has suggested that the smallest-level nanocrystalline apatite complexes in bone possessing non-collagenous proteins are responsible for its exceptional elasticity (i.e., via temporary pile-up). Consequently, these complexes produce an extension of the contact area against high-strain-rate mechanical stimuli such that mature bone can resist the initiation of microcracks via its enhanced resilience [6,7]. The smallest structural unit of enamel is also nanocrystalline hydroxyapatite, bundled together with non-collagenous protein glues [8], and so even enamel, which is the most highly organized mineralized composite, could exhibit this behavior.

The stress–strain response is a basic parameter related to several mechanical properties (and limits) of a material. The elastic–plastic transition point (i.e., elastic limit) of a material provides important insight into the deformability of a material before fracture because the initiation of microcracks always occurs beyond the elastic limit. The elastic limit also represents the strain energy storage within the elastic range (i.e., resilience). At the smallest length scale, the elastic–plastic transition of enamel with increasing stress may be caused by frictional sliding between the nanocrystals or by detachment of the protein glues, because the tiny enamel crystals may not be plastically deformable [9]. Assuming that the enamel contact mechanics are variable with external loading strain rates, as has been observed in cortical bone [7,10], the extension of the contact area (during high-loading strain) prevents this interfacial slippage of the crystals, thus inducing their enhanced elastic limit and remarkable resilience.

We hypothesized a strain-rate-dependent enhanced elastic limit of tooth enamel at the smallest scale that allows remarkable resilience against high strain rates. We quantified the stress–strain behavior of human tooth enamel at various nanoindentation loading rates using indenter tips with radii of 243 and 1041 nm. A superimposed signal amplitude (1–2 nm) embedded in the loading component of a single force–displacement curve was used to continuously capture the enamel contact stiffness for different loading strain rates [11]. The models chosen to interpret the strain rate extension of the contact area below the elastic limit were (i) the 'quasi-static' elastic modulus below the elastic limit according to the classical Hertzian contact theory [12], and (ii) the storage modulus generated during 'dynamic' nanoindentation loading strain [13]. The quasi-static elastic modulus calculated by (i) relies on the indenter penetration depth, while the storage modulus in (ii) takes into account the contact stiffness associated with the indentation contact area (see Section 2). Variations in the elastic moduli determined from (i) and (ii) signify that strain-rate-dependent mechanical behavior of enamel lies beyond the quasi-static elastic contact theory, which ultimately results in exceptional contact elasticity and consequent enhanced elastic limit. Thus, a nanoscale origin of enamel durability could be suggested by this study.

2. Materials and methods

2.1. *Specimen preparation*

Human third molar teeth were extracted (for orthodontic indications) under a protocol approved by the Ethics Committee of the School of Dentistry, Showa University (Ref.: 2014-031). The specimens were stored in Hank's Balanced Salt Solution (Sigma-Aldrich, USA) until required for testing, which minimized near-surface demineralization and any subsequent changes in their mechanical properties [14]. Before measurements, the cuspal region of the tooth was cut horizontally and polished with silicon carbide paper (#800–1000) (Fig. A.1 in Supplementary material) to perpendicularly expose keyhole-shaped structures corresponding to microscale enamel rods and their surrounding protein-rich sheaths at the surface (Fig. 1A). The enamel was further polished with 0.3–0.05 μm alumina polishing paste (Buehler, USA) to prepare a refined surface suitable for use in atomic force microscopy (AFM) and nanoindentation tests.

2.2. *Nanoindentation*

Prior to each set of indentation tests, the polished tooth sample was briefly submerged in Hank's Solution. To maintain moist (partially hydrated) conditions, each test was completed within 60 min [9]. The nanoindentation experiments were performed in the central regions of the enamel rods using a quantitative nanomechanical testing instrument (TI 950 TriboIndenter; Hysitron, Inc., USA) interfaced with an AFM. Fused quartz (Hysitron Inc.) was used as the standard calibration material. Diamond spherical-tipped indenters with tip radii of 243 and 1041 nm were chosen for this study. The effective indenter tip radii (i.e., calibrated tip radii) were determined from preliminary depth-dependent loading/partial unloading tests on fused quartz (E_r = 69.7 GPa) [15]. The technique used a load function containing a total of 20 partial unloading cycles, each comprising a 1 s loading segment, a 1 s hold segment, and a 1 s unloading segment to maximum loading forces of 250 and 2000 μN for the indenter tip radii of 243 and 1041 nm, respectively (see Appendix A in Supplementary material). Continuous nanodynamic–mechanical measurements (Nano

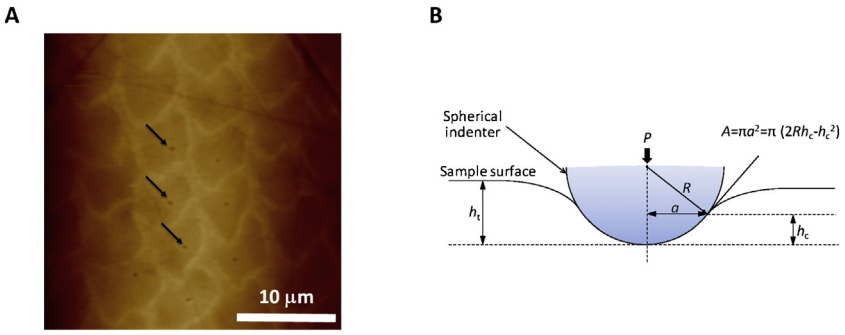

Fig. 1 – Nanoindentation tests of enamel rods. (A) Representative atomic force microscope image of polished enamel surface. Indentation points are marked with arrows. (B) Schematic diagram of elastic contact between a spherical indenter and the material surface, showing the applied load (*P*), indenter radius (*R*), radius of the indentation area (*a*), total indentation depth (h_t), and contact depth (h_c). In the elastic range, $h_c = h_t/2$.

DMA-III interfaced with a TI 950 TriboIndenter, Hysitron Inc.) were obtained from the fused quartz and the enamel rods.

A force–displacement curve with constant strain rate loading followed by 5 s holding was recorded using strain rates of 0.031, 0.041, and 0.061 s^{-1} (Fig. 2A) to produce maximum loads of 250 and 2000 μN for the indenter tip radii of 243 and 1041 nm, respectively. Sinusoidal oscillations at a frequency of 220 Hz and signal amplitude of 1–2 nm were superimposed on these curves [11].

Using the fused quartz data, we plotted the strain, as measured by *a*/R, as a function of time. The data displayed an almost constant increase of strain at each indentation loading rate for a spherical indenter (Fig. 2B).

2.2.1. *Stress–strain behavior*

Indentation-derived stress–strain curves were introduced by Tabor [16], wherein the indentation contact area (A) is related to the indentation radius (*a*) or to the indenter radius (R) and the contact depth (h_c) (Fig. 1B), such that

$$A = \pi a^2 = \pi(2Rh_c - h_c{}^2) \tag{1}$$

The Hertzian equation for the elastic contact of an elastically isotropic material is given by [17]

$$h_t = \left(\frac{9}{16}\right)^{1/3}\left(\frac{P}{E_r}\right)^{2/3}\left(\frac{1}{R}\right)^{1/3} \tag{2}$$

where h_t is the total penetration depth, *P* is the applied load, and E_r is the reduced elastic modulus.

In the elastic regime, which is typically the case during the onset of loading,

$$h_c = \frac{h_t}{2} \tag{3}$$

The initial parts of the loading curves were fitted with Eq. (2) to obtain the radius of curvature of each indenter. These were determined within the linear behavior of h_t versus $P^{2/3}$ and the limit of the elastic range [9,15].

Nanoindentation analyses should be performed on the basis of an ideal contact between the indenter tip and a perfectly polished uniform surface, but these conditions are highly unlikely at the nanoscale for biological samples during initial contact. Such inaccurate initial contact often results in an overestimation of the total indenter penetration depth, h_t [18]. Based on the assumption that the origin of the linear fit of h_t versus $P^{2/3}$ must be zero within the elastic range, we corrected these data by introducing offsets of the h_t value (Fig. A.2 in Supplementary material). This gave accurate data analysis throughout this study.

Previous works have reported an equivalence between the conventional stress–strain responses and the curves generated by plotting the mean contact pressure (P_m) against the contact radius divided by the effective indenter radius (*a*/R) when using a spherical-tipped indenter [9,15]. The mean contact pressure P_m can be calculated as

$$P_m = \frac{P}{A} \tag{4}$$

where the indentation contact area (A) is the projected contact area obtained from Eqs. (1)–(3) [19].

2.2.2. *Elastic modulus*

The loading portions of the nanoindentation load–displacement data were used to derive indentation stress–strain curves. The reduced elastic modulus, E_r, was calculated using Eq. (2) at each data point and the slope at the onset of the stress–strain curve (quasi-static elastic modulus).

By substituting Eqs. (1)–(3) into Eq. (4), the elastic regime of the stress–strain curve can be described as

$$P_m = \left(\frac{4E_r}{3\pi}\right)\frac{a}{R} \tag{5}$$

where *a*/R is the contact strain during elastic loading of the material and $4E_r/3\pi$ is the slope [15]. From Eq. (5), a quasi-static elastic modulus from the slope angle of the stress–strain curve can be calculated as

$$E_r = 3\pi\frac{k}{4} \tag{6}$$

The indenter tip also simultaneously captured the frequency-dependent loss tangent (tan δ) and strain-dependent effective modulus (i.e., storage *E*′). A tiny signal amplitude at 220 Hz,

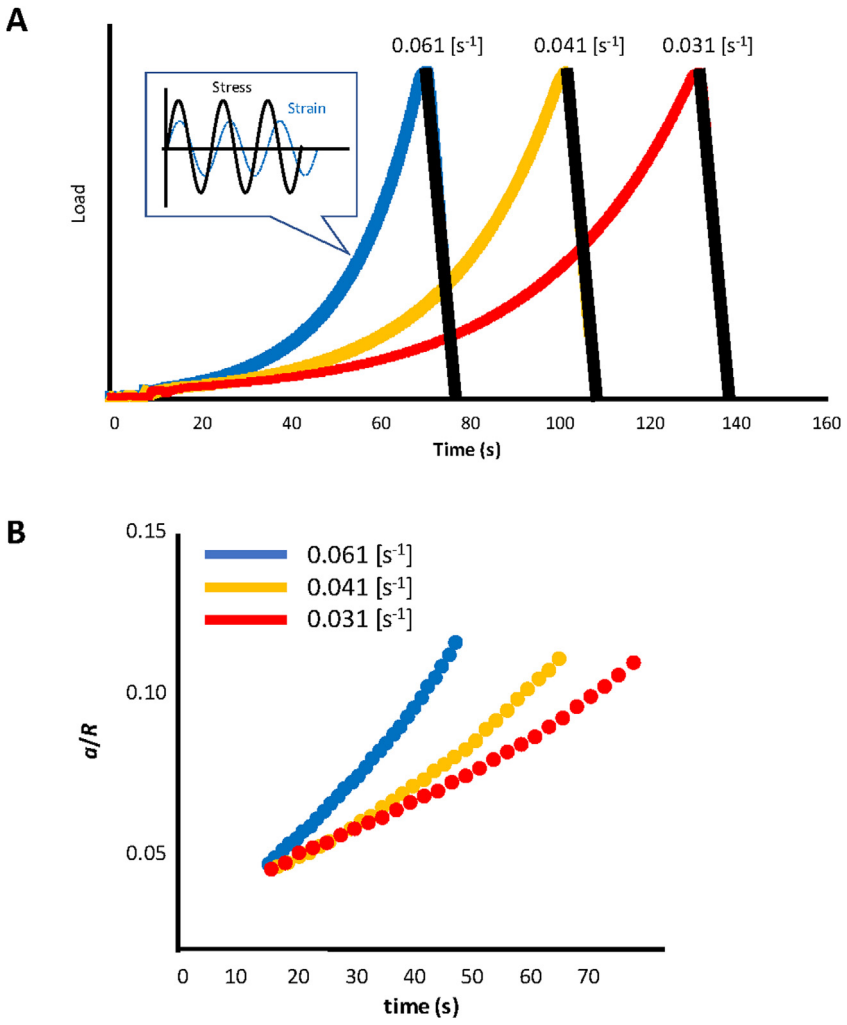

Fig. 2 – Nanoindentation experiments at various strain rates. (A) Indentation load functions used in this study. A superimposed signal amplitude of 1–2 nm at a frequency of 220 Hz during the loading portion (colored lines) of the function enabled continuous measurement of contact stiffness. (B) Strain (*a*/*R*) versus time curves at each loading strain rate obtained from the spherical indenter with a radius of 1041 nm. (For interpretation of the references to color in this figure legend, the reader is referred to the web version of this article.)

embedded within the quasi-static loading, assessed both elastic and viscoelastic properties. The calculated elastic modulus (storage modulus) for each test was therefore corrected by subtracting the viscoelastic response (loss modulus E″).

During superimposed dynamic sinusoidal oscillations, a phase lag existing between the applied stress and the measured strain signal indicates viscoelastic behavior. For an elastic solid, the resulting stress and strain should be completely in phase, while a Newtonian viscous fluid exhibits a 90° phase lag in strain with respect to the applied stress [20]. The tangent of the phase lag (tan δ) in Eq. (7) is the ratio of the storage modulus (E′) to the loss modulus (E″), as described by Ref. [13]:

$$\tan\delta = \frac{E''}{E'} \tag{7}$$

$$E' = \frac{S_e\sqrt{\pi}}{2\sqrt{A}} \tag{8}$$

$$S_e = \frac{\sigma_0}{\varepsilon_0}\cos\delta \tag{9}$$

where S_e is the storage contact stiffness, σ_0 is the stress amplitude, ε_0 is the strain amplitude, and δ is the phase lag (in radians). A correction for the elastic (i.e., storage) modulus determination can be made using the indentation contact area (A) and substituting Eq. (9) into Eq. (8).

2.2.3. *Modulus mapping*

Quantitative modulus maps of the enamel rods in the form of AFM images (10 μm × 10 μm) were acquired using the direct-force modulation (nano DMA III) operating mode of the nanoindenter. The electrostatic force acting on the spring-suspended center plate of the force–displacement transducer of the nanoindenter was sinusoidally modulated at 220 Hz during contact-mode imaging. A spherical indenter (radius of 1041 nm) was attached to this transducer. The amplitude of displacement was maintained at 0.4–1.0 nm and the phase of

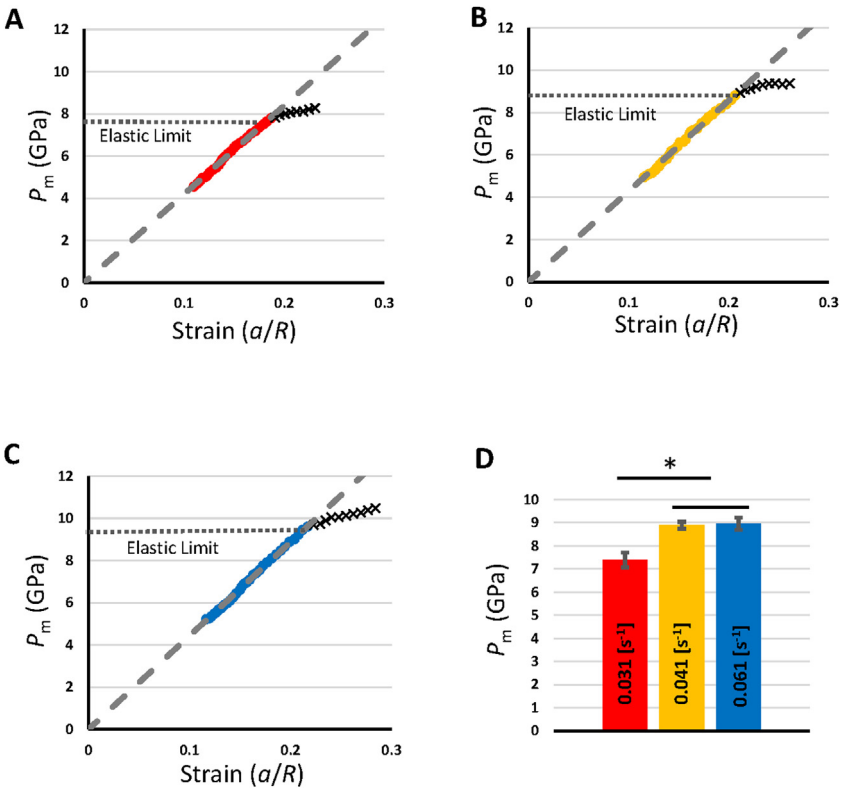

Fig. 3 – Stress–strain curves of enamel for the smaller indentation contact range ($a \sim 50$ nm contact radius). (A–C) Representative stress–strain curves at loading strain rates of (A) 0.031, (B) 0.041, and (C) 0.061 s^{-1}. (D) Average observed elastic limits at each loading strain rate. The results are expressed as the mean ± standard deviation (six indentation tests on the same sample surface, $n = 6$). A value of $p < 0.05$ was considered significant (*). Different teeth showed similar tendencies, irrespective of varied properties related to their structural heterogeneity.

the resulting transducer displacement signal was measured with a dual-channel lock-in amplifier. This phase information was used to determine the local indentation modulus of the sample at each pixel of the imaging process. This modulus mapping technique was calibrated using the fused quartz standard to determine the tip contact radius necessary to achieve an appropriate sample displacement [21]. When imaging in the direct-force modulation mode, the nominal contact force was determined solely by the transducer spring deflection. The amplitude of the modulated electrostatic force was set to 4 μN with a tip velocity of 0.05 μm s^{-1}, which was sufficiently large to maintain a good signal-to-noise ratio for enamel and fused quartz while sufficiently small to prevent intermittent contact. Signals corresponding to the nominal contact force, the displacement amplitude, the displacement phase, and the topography were recorded at each of the 256 × 256 pixels of the imaging process. The storage and loss components of the complex contact stiffness were extracted from the spatially correlated set of amplitude and phase images to generate quantitative stiffness maps. The storage modulus (E') was determined from Eqs. (7)–(9).

2.3. *Statistical analysis*

At least six nanoindentation regions on same sample surface were assessed for the stress–strain analysis. Six sets of randomly selected linear analysis data on same sample surface were collected from modulus mapping and analyzed using *ANOVA* software (BellCurve for Excel, Social Survey Research Information Co., Ltd., Tokyo, Japan) to run Tukey post hoc tests, wherein p values of less than 0.05 were considered statistically significant. Representative mean values obtained from a single tooth are shown in the data presented in Section 3. Similar tendencies of these indentation tests were confirmed for different teeth.

3. Results

3.1. *Stress–strain curves*

The stress–strain curves on enamel exhibited a linear elastic response. The limit of the elastic range was approximated from the region of the curve that did not deviate from linearity. For the smaller contact range indentation tests (i.e., $a \sim 50$ nm contact radius), the mean contact pressure, P_m, observed in the stress–strain curves at the elastic limits was 7–9 GPa (Fig. 3). The corresponding elastic limit in the smaller indentation contact range significantly increased ($p < 0.05$) with the loading strain rate (Fig. 3D).

For the larger contact range indentation tests (i.e., $a \sim 150$ nm contact radius), the observed mean contact pressure at the elastic limit at the lowest loading strain rate was

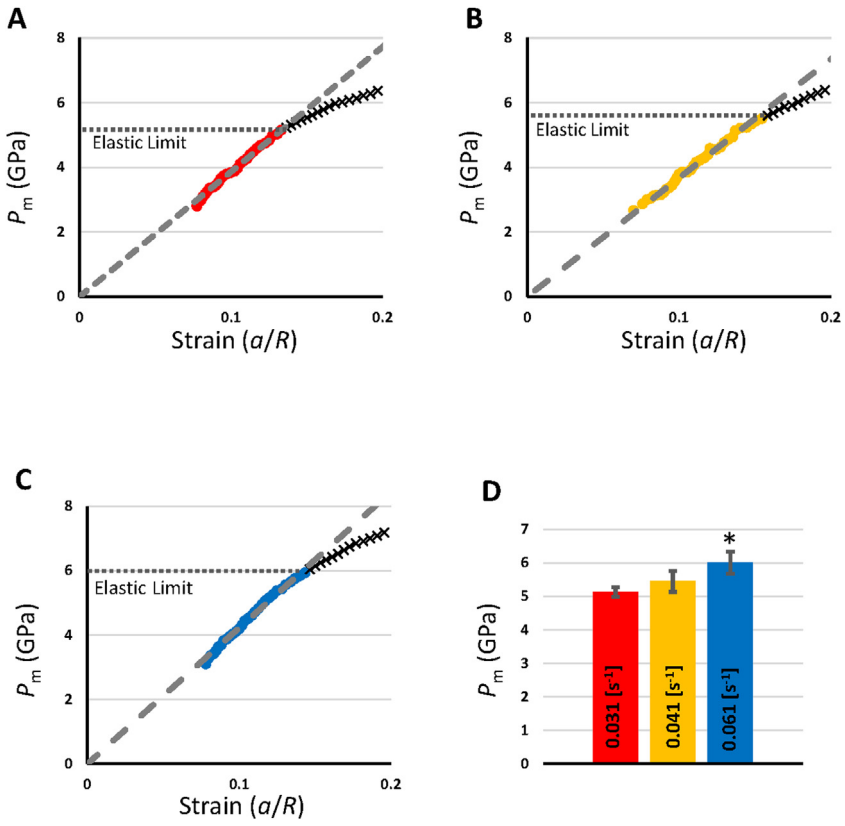

Fig. 4 – Stress–strain curves of enamel at the larger indentation contact range ($a \sim 150$ nm contact radius). (A–C) Representative stress–strain curves at loading strain rates of (A) 0.031, (B) 0.041, and (C) 0.061 s^{-1}. (D) Average observed elastic limits at each loading strain rate. The results are expressed as the mean ± standard deviation (six indentation tests on sample surface, $n = 6$). A value of $p < 0.05$ was considered significant (*). Different teeth showed similar tendencies, irrespective of varied properties related to their structural heterogeneity.

around 5 GPa, whereas that corresponding to the highest loading strain rate was 6 GPa (Fig. 4). The mean contact pressure at the elastic limit was significantly higher ($p < 0.05$) at the high-loading strain rate than that at the lower strain rates (Fig. 4D). Furthermore, the highest elastic limit in this contact range was significantly lower ($p < 0.05$) than those observed in the smaller contact range indentation tests (Fig. 3D).

3.2. *Effect of quasi-static loading strain rate on elastic modulus*

The storage moduli in the smaller indentation contact range, obtained from the superimposed signal amplitudes during loading, were approximately 150 GPa (Fig. 5A–C). These were significantly higher ($p < 0.05$) than the quasi-static elastic moduli.

The storage moduli in the larger indentation contact range, corresponding to the superimposed dynamic amplitude during loading, were approximately 130 GPa, which was also significantly higher ($p < 0.05$) than the quasi-static elastic moduli (Fig. 5D–F). The storage moduli in the larger indentation contact range were significantly lower ($p < 0.05$) than those in the smaller indentation contact range. The quasi-static elastic moduli were around 100 GPa and were equivalent ($p > 0.05$) for both indenter contact ranges (Fig. 5). Furthermore, they were statistically equivalent ($p > 0.05$) to those calculated by the slope angle of the linear portion at the onset of the stress–strain curves (Fig. A.3 in Supplementary material). Each quasi-static and storage modulus value remained constant irrespective of the contact depth and/or strain rate (Fig. 5) ($p > 0.05$). The storage modulus of fused quartz was approximately 70 GPa throughout this series of indentation tests (not shown). This value was statistically invariable ($p > 0.05$) from the value obtained from quasi-static theory.

An AFM topographical map (10 μm × 10 μm area) obtained from the modulus mapping showed enamel rods and protein-rich sheath layers (Fig. 6A). The average storage modulus for the enamel rods was 59.06 GPa (Fig. 6C), which was significantly lower ($p < 0.05$) than the values obtained from quasi-static theory and those calculated considering dynamic contact stiffness (Fig. 5).

4. Discussion

We present data demonstrating strain-rate-dependent contact elasticity and the consequent elastic limit of human tooth enamel at the smallest level. The primary objective of this nanoindentation study was to explore the intrinsic stress–strain response of enamel in relation to the nanoscale structural unit corresponding to different *in situ* loading strain rates.

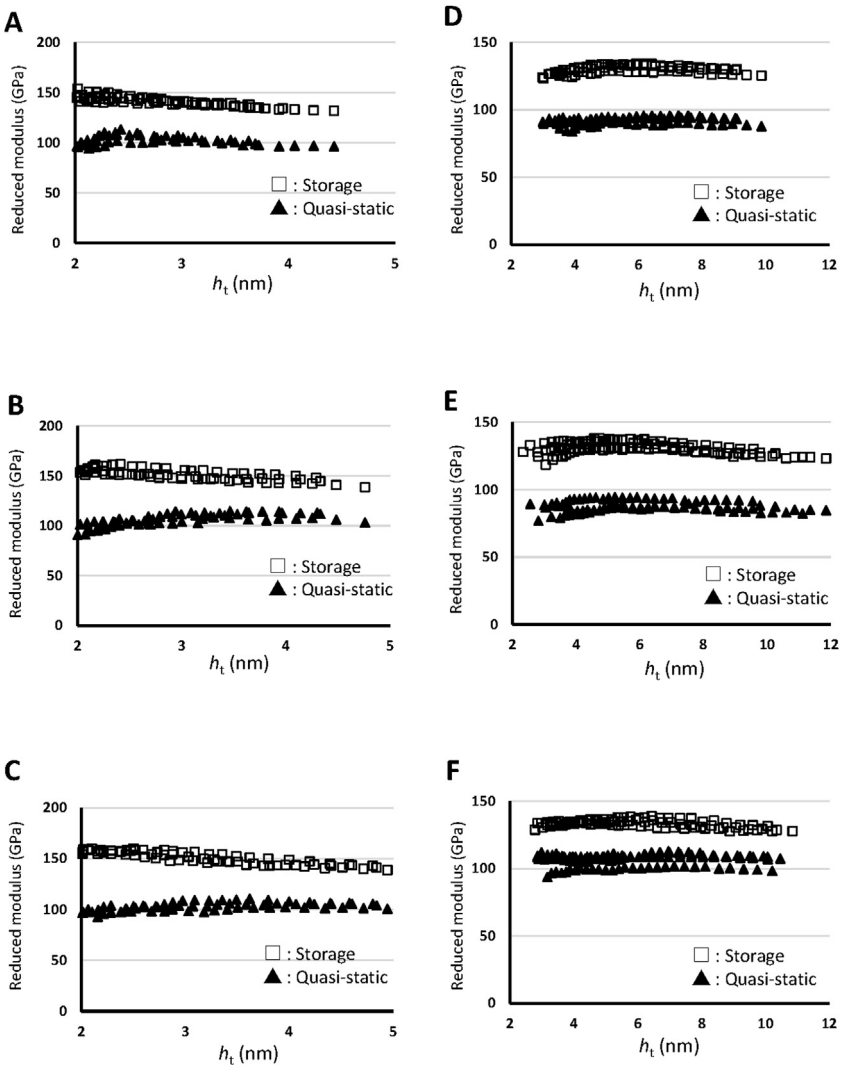

Fig. 5 – Elastic modulus for the smaller indentation contact range ($a \sim 50$ nm contact radius) at loading strain rates of (A) 0.031, (B) 0.041, and (C) 0.061 s^{-1}. Elastic modulus for the larger indentation contact range ($a \sim 150$ nm contact radius) at loading strain rates of (D) 0.031, (E) 0.041, and (F) 0.061 s^{-1}. The panels plot the storage moduli obtained from the superimposed signal amplitude embedded during quasi-static indentation loading (square points) and the elastic moduli obtained from quasi-static theory (triangles). The plots show at least three sets of indentation data obtained below the observed elastic limits. A value of $p < 0.05$ was considered significant (six indentation tests on the same sample surface, $n = 6$). Different teeth showed similar tendencies, irrespective of varied properties related to their structural heterogeneity.

Indentation testing on biological materials is not always independent of size-dependent properties. For tooth enamel, the elastic modulus reduces with increasing indentation contact area because a larger contact area is more sensitive to the "soft" sheath protein surrounding the micrometer-scale enamel rods [22] (Figs. 1A and 6A). The constant elastic moduli observed within the target measurement ranges (~50 and ~150 nm contact radii) of the two spherical indenters revealed that our nanoindentation test was able to assess the mechanical properties of enamel without the influence of a size-dependent property. The theoretical length scale of these contact ranges incorporates multiple enamel nanocrystals and the remnant protein glue within the enamel rod [1,9,23].

In addition, the depth-dependent property present in layered materials often causes a variable elastic modulus (depending upon indenter radius), which can be measured by the slope angle obtained from the stress–strain curve, in comparison with the moduli detected at each data point [24,25]. The almost equivalent elastic moduli determined from the above two quasi-static measurement theories indicated that these nanoindentation tests revealed a homogeneous enamel structure with respect to the depth, at least below the elastic limit.

The observed mechanical response of fused quartz was always measured at about 70 GPa and was independent of the loading strain rate, because the isotropic amorphous structure of fused quartz enables this virtually time-independent

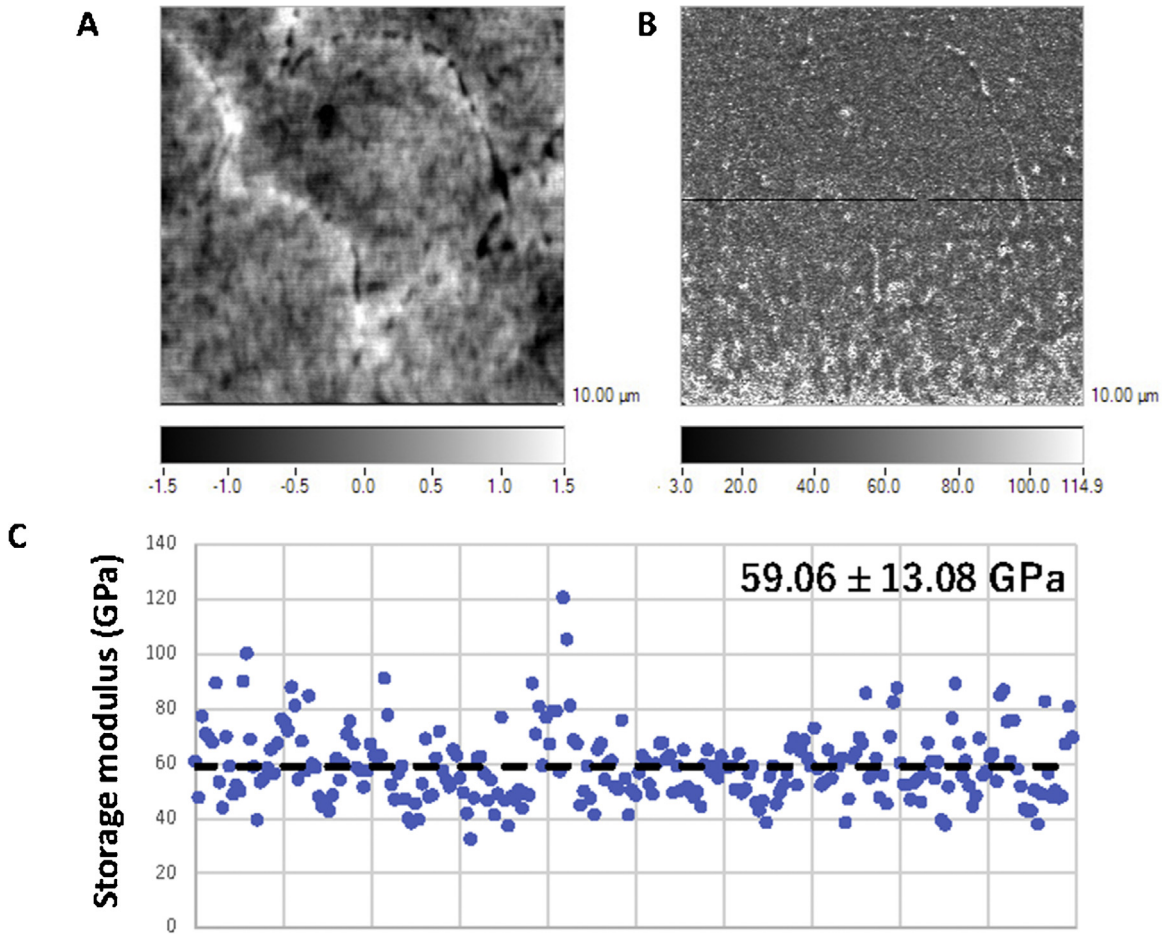

Fig. 6 – Modulus mapping of an enamel rod. (A, B) Intensity plots of enamel rod mapping of (A) contact force (units of μN) and (B) storage modulus (units of GPa). (C) Representative storage modulus values across the width of an enamel rod. The data are the average of six sets of randomly selected average linear analysis data ± standard deviation. Different teeth showed similar tendencies, irrespective of varied properties related to their structural heterogeneity.

property. The strain-rate-dependent mechanical properties of the tooth enamel observed in the present study could be associated with exceptional contact elasticity, and specifically with the strain-rate-dependent property of the nanocrystalline apatite and protein glue complex against indentation strains.

4.1. *Elastic modulus*

During dynamic nanoindentation loading strains, we measured the quasi-static elastic moduli as a function of the storage moduli below the elastic limits; however, the presence of the superimposed dynamic (signal) amplitude made it difficult to conclude whether the storage modulus corresponded to the primary quasi-static loading strain or the high-frequency superimposed amplitude. Modulus mapping was capable of capturing signal amplitudes of <1 nm during AFM observation without an increase of the loading force (see Section 2). Accordingly, modulus mapping can be theoretically considered as an indentation test having an extremely low quasi-static loading strain rate (≈ 0). The average storage modulus obtained from modulus mapping was around 60 GPa, which was lower than the values obtained from quasi-static indentation analysis (100 GPa) and from indentation loading (130–150 GPa). As such, the superimposed signal amplitude alone does not appear to play an integral role in the enhanced storage moduli. In this context, the storage moduli measured by the strain rate indentation tests were most likely dependent on the foundational loading strain rather than the tiny amplitude of the superimposed signal.

According to Eqs. (1)–(3), the quasi-static elastic moduli measured on enamel depend on the contact depth (see Section 2) that is determined by the Hertzian elastic contact theory, where $h_c = h_t/2$ (Figs. 1B and 7). Because the temporary pile-up (elastic range) response resists indenter penetration [7,10], this would reduce the contact depth and thus enhance the elastic modulus during loading strain. The lack of temporary pile-up response in modulus mapping results in the lowest inelastic property.

Based on Eq. (8), the storage modulus on enamel was calculated from the contact (i.e., storage) stiffness as a function of the contact area (see Section 2). The enhanced storage moduli were suggestive of increased contact stiffness with an extension of the "true" contact area with increased loading strain rates, while the theoretical contact area substituted for Eq. (8) was underestimated by the Hertzian contact theory (Figs.

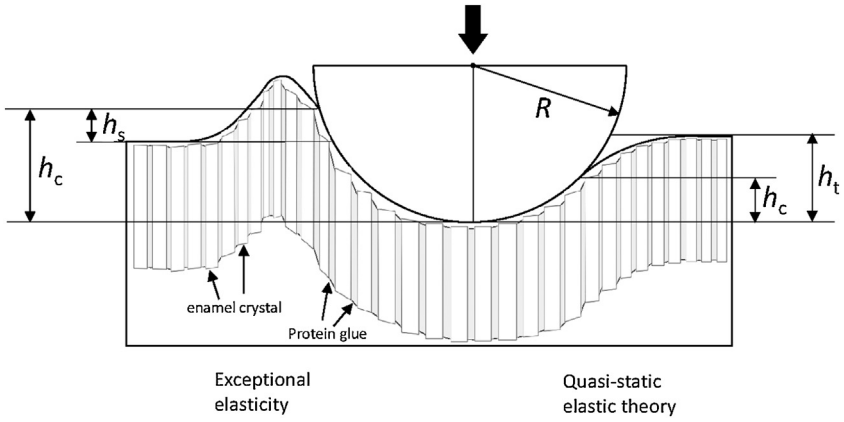

Fig. 7 – Schematic illustration (adapted from Ref. [9]) of the exceptional elastic response (left) and estimated theoretical elastic deformation (right) of enamel induced by a spherical indenter. Shown are the indenter tip radius (*R*), total penetration depth (h_t), contact depth (h_c), and (temporary) pile-up depth (h_s). The *h* values are much smaller than *R* in reality. An extension of the contact area prevents frictional sliding between nanocrystals or detachment of protein glues, and thus an enhanced elastic limit occurs (left). An enhanced contact stiffness via an increase of true contact area (left) as a function of the estimated contact area calculated from quasi-static elastic theory (right) results in an apparent high elastic modulus.

1B and 7). As such, the apparent inelastic response observed for plots of the storage moduli against the loading strain was much higher than that measured by the quasi-static theory wherein contact stiffness was not taken into account.

The variations in the values of the elastic moduli determined from the different methods (modulus mapping < quasi-static theory modulus < storage modulus) suggested an increase of the temporary pile-up response on enamel in line with the primary quasi-static loading strain. Variation of the storage moduli with quasi-static loading strain rate was less significant, but the simultaneously observed enhanced elastic limits also signified a potential temporary pile-up response that would diminish interfacial slippage of the enamel nanocrystals via extension of the contact area (Fig. 7).

4.2. *Nanoscale exceptional contact elasticity of enamel*

The estimated contact range for modulus mapping was much smaller than that determined through the nanoindentation tests using spherical-tipped indenters: the theoretical length scale of this contact range corresponds to single-crystal enamel, while the reduced elastic modulus of pure hydroxyapatite has been previously reported as ~130 GPa [26,27]. Despite the high degree of contact with single crystals, the value observed in the modulus mapping test was much lower than that of pure hydroxyapatite. The mechanical behavior of enamel, such as the time-dependent response of (soft) protein glue, is always a contributing factor.

Strain-rate-dependent nanoscale exceptional contact elasticity has been recently observed in the smallest structure of bone [7,10]. According to the theory advocated in these studies, a substantial shear strain is generated parallel to the indenter tip/enamel interface in the presence of high loading strain rates. Under shear displacement, most time-dependent materials expand in the direction perpendicular to the applied shear stress [1,28,29]. Through this dilatational behavior, deformation primarily occurs perpendicular to the direction of indenter penetration into the enamel surface, resulting in exceptional elastic deformation (temporary pile-up) of tissue around the indenter tip, thereby increasing the contact stiffness owing to extension of the contact area (Fig. 7).

This temporary pile-up response at the smallest level is most predominant in the smaller contact range indentation tests. Thus, an apparently enhanced storage modulus and consequent increase of the elastic limit were more prominent in the smaller contact range indentation tests than in the larger contact range. The strain-rate-dependent elastic limits observed in the larger contact range indentation tests may be related to delayed viscoelastic deformation of the protein glue because, theoretically, the sensitivity of the delayed response of biominerals increases with contact range [22]. However, the various elastic moduli measured for the different theoretical considerations, even in the larger indentation contact range, also suggest a temporary pile-up response that can lead to an increase in the elastic limit owing to extension of the contact area during high-loading strain rates.

The stress intensity at a microcrack can be weakened by the delayed response of the protein glue that exhibits time-dependent viscoelasticity [30,31]. Although viscoelastic creep behavior is thought to be responsible for enamel toughness [27,32], this delayed response of the enamel cannot be fully responsible for the high strain rates that occur during occlusal contacts. In addition, enamel must have remarkable resilience at the smallest structural level to prevent initiation of microcracks, which is a consequence of extra energy expenditure via exceptional elasticity against high strain rates.

It is noteworthy that this primary dynamic mechanical behavior lies well beyond what can be described using quasi-static elastic contact theories. In this context, all of the measured values in the present study cannot be simply compared with those previously reported for time-independent materials, such as metals or ceramics.

4.3. *Outlook*

With the development of high-resolution indentation devices, new methods are available to measure the localized mechanical properties of biominerals, such as bone, tooth, and nacre [19,33,34]. Although the indentation technique has a long history of use in characterizing the mechanical behavior of materials [15–17,19,33], these studies were based on the classical Hertzian contact theory that neglects the time-dependent exceptional elastic deformation that is inherent to the indentation of biological materials. Biominerals, such as tooth enamel, cannot be fully described using quasi-static elastic contact theories: this should be taken into consideration when evaluating the material properties of biominerals. To overcome these limitations, the quasi-static and dynamic indentation protocol introduced in this study may be used.

5. Conclusion

We observed an enhanced elastic limit of tooth enamel arising from its exceptional contact elasticity at the nanoscale (i.e., material) level. Extension of the contact area and the consequent increase of the elastic limit allows remarkable resilience corresponding to high loading strains. This may provide useful insights for conceptualizing advanced biomaterials. The present study also provides a comprehensive and precise protocol for the mechanical characterization of biominerals and/or bio-inspired nanocomposites.

Data availability

The data that support the findings of this study are available from the corresponding author upon reasonable request.

Acknowledgements

This work was supported by the Fund for the Promotion of Joint International Research (16KK0209) and a Grant-in-Aid for Scientific Research (C: 16K11563) from the Ministry of Education, Culture, Sports, Science and Technology of Japan. We thank Shofu Inc. for financial support. We also thank Kathryn Sole, PhD, from Edanz Group (www.edanzediting.com/ac) for editing a draft of this manuscript.

Appendix A. Supplementary data

Supplementary data associated with this article can be found, in the online version, at https://doi.org/10.1016/j.dental.2018.11.005.

REFERENCES

[1] Bar-On B, Wagner H. Structural motifs and elastic properties of hierarchical biological tissues — a review. J Struct Biol 2013;183:149–64.
[2] He LH, Swain MV. Understanding the mechanical behaviour of human enamel from its structural and compositional characteristics. J Mech Behav Biomed Mater 2008;1:18–29.
[3] Olszta MJ, Cheng X, Jee SS, Kumar R, Kim YY, Kaufman MJ, et al. Bone structure and formation: a new perspective. Mater Sci Eng R Rep 2007;58:77–116.
[4] Koenigswald WV, Clemens WA. Levels of complexity in the microstructure of mammalian enamel and their application in studies of systematics. Scanning Microsc 1992;6:195–218.
[5] Bechtle S, Ang SF, Schneider GA. On the mechanical properties of hierarchically structured biological materials. Biomaterials 2010;31:6378–85.
[6] Poundarik AA, Diab T, Sroga GE, Ural A, Boskey AL, Gundberg CM, et al. Dilatational band formation in bone. Proc Natl Acad Sci U S A 2012;109:19178–83.
[7] Maruyama N, Shibata Y, Mochizuki A, Yamada A, Maki K, Inoue T, et al. Bone micro-fragility caused by the mimetic aging processes in α-klotho deficient mice: in situ nanoindentation assessment of dilatational bands. Biomaterials 2015;47:62–71.
[8] Macho GA, Jiang Y, Spears IR. Enamel microstructure — a truly three-dimensional structure. J Hum Evol 2003;45:81–90.
[9] Ang SF, Bortel EL, Swain MV, Klocke A, Schneider GA. Size-dependent elastic/inelastic behavior of enamel over millimeter and nanometer length scales. Biomaterials 2010;31:1955–63.
[10] Maruyama N, Shibata Y, Wurihan A, Swain MV, Kataoka Y, Takiguchi Y, et al. Strain-rate stiffening of cortical bone: observations and implications from nanoindentation experiments. Nanoscale 2014;6:14863–71.
[11] Miyamoto S, Miyamoto Y, Shibata Y, Yoshimura K, Izumida E, Suzuki H, et al. In situ quasi-static and dynamic nanoindentation tests on calcified nodules formed by osteoblasts: implication of glucocorticoids responsible for osteoblast calcification. Acta Biomater 2015;12:216–26.
[12] Lawn BR. Indentation of ceramics with spheres: a century after Hertz. J Am Ceram Soc 1998;81:1977–94.
[13] Herbert EG, Oliver WC, Pharr GM. Nanoindentation and the dynamic characterization of viscoelastic solids. J Phys D Appl Phys 2008:41.
[14] Habelitz S, Marshall Jr GW, Balooch M, Marshall SJ. Nanoindentation and storage of teeth. J Biomech 2002;35:995–8.
[15] Field JS, Swain MV. A simple predictivity model for spherical indentation. J Mater Res 1993;8:297–306.
[16] Tabor D. The hardness of metals. Oxford: Clarendon Press; 1951.
[17] Hertz HR. Miscellaneous papers. London: Macmillan; 1896.
[18] Basu S, Moseson A, Barsoum MW. On the determination of spherical nanoindentation stress–strain curves. J Mater Res 2006;21:2628–37.
[19] Oliver WC. An improved technique for determining hardness and elastic modulus using load and displacement sensing indentation experiments. J Mater Res 1992;7:1564–83.
[20] Sanctuary CS, Wiskott HWA, Justiz J, Botsis J, Belser UC. In vitro time-dependent response of periodontal ligament to mechanical loading. J Appl Physiol 2005;99:2369–78.
[21] Cuy JL, Mann AB, Livi KJ, Teaford MF, Weihs TP. Nanoindentation mapping of the mechanical properties of human molar tooth enamel. Arch Oral Biol 2002;47:281–91.
[22] He LH, Fujisawa N, Swain MV. Elastic modulus and stress–strain response of human enamel by nano-indentation. Biomaterials 2006;27:4388–98.
[23] Staines M, Robinson WH, Hood JAA. Spherical indentation of tooth enamel. J Mater Sci 1981;16:2551–6.
[24] Bushby AJ, Ferguson VL, Boyde A. Nanoindentation of bone: comparison of specimens tested in liquid and embedded in polymethylmethacrylate. J Mater Res 2004;19:249–59.

[25] Basu S, Barsoum MW, Williams AD, Moustakas TD. Spherical nanoindentation and deformation mechanisms in freestanding GaN films. J Appl Phys 2007;101.
[26] He LH, Standard OC, Huang TTY, Latella BA, Swain MV. Mechanical behaviour of porous hydroxyapatite. Acta Biomater 2008;4:577–86.
[27] He LH, Swain MV. Enamel-A "metallic-like" deformable biocomposite. J Dent 2007;35:431–7.
[28] Dobrynin AV, Carrillo JMY. Universality in nonlinear elasticity of biological and polymeric networks and gels. Macromolecules 2011;44:140–6.
[29] Storm C, Pastore JJ, MacKintosh FC, Lubensky TC, Janmey PA. Nonlinear elasticity in biological gels. Nature 2005;435:191–4.
[30] Cristofolini L, Viceconti M, Cappello A, Toni A. Mechanical validation of whole bone composite femur models. J Biomech 1996;29:525–35.
[31] Ji B, Gao H. Mechanical properties of nanostructure of biological materials. J Mech Phys Solids 2004;52:1963–90.
[32] He LH, Swain MV. Influence of environment on the mechanical behaviour of mature human enamel. Biomaterials 2007;28:4512–20.
[33] Oliver WC, Pharr GM. Measurement of hardness and elastic modulus by instrumented indentation: advances in understanding and refinements to methodology. J Mater Res 2004;19:3–20.
[34] Suganuma M, Swain MV. Simple method and critical comparison of frame compliance and indenter area function for nanoindentation. J Mater Res 2004;19:3490–502.